Femtosecond second-harmonic generation in AlGaAs Bragg reflection waveguides: theory and experiment

J. B. Han,[1] P. Abolghasem,[1] B. J. Bijlani,[1] A. Arjmand,[1] S. Chaitanya Kumar,[2] A. Esteban-Martin,[2] M. Ebrahim-Zadeh,[2,3] and A. S. Helmy[1,*]

[1]*The Edward S. Rogers Sr. Department of Electrical and Computer Engineering, University of Toronto, 10 King's College Road, Toronto, Ontario M5S 3G4, Canada*
[2]*ICFO–Institut de Ciencies Fotoniques, Mediterranean Technology Park, Castelldefels (Barcelona) 08860, Spain*
[3]*Institucio Catalana de Recerca i Estudis Avancats (ICREA), Passeig Lluis Companys 23, Barcelona 08010, Spain*
**Corresponding author: a.helmy@utoronto.ca*

Received February 18, 2010; accepted April 9, 2010;
posted April 22, 2010 (Doc. ID 124463); published May 24, 2010

The impact of third-order nonlinearities including self-phase modulation and two-photon absorption on the efficiency of the second-harmonic generation is numerically investigated using the split-step Fourier method in phase-matched Bragg reflection waveguides. Also using the same technique, the adverse effects of group velocity mismatch and group velocity dispersion of the interacting frequencies on the efficiency of the nonlinear process are examined and contrasted for optimal sample design. Using an optimized structure, we report efficient femtosecond second-harmonic generation in monolithic AlGaAs Bragg reflection waveguides for a type II nonlinear interaction. For a 190 fs pulsed pump around 1555 nm with an average power of 3.3 mW, a peak second-harmonic power of 25.5 μW is measured in a sample with a length of 1.1 mm. The normalized conversion efficiency of the process is estimated to be $2.0\times10^{4}\%$ W^{-1} cm^{-2}. Pump depletion is clearly observed when operating at the phase-matching wavelength.

OCIS codes: 230.7370, 230.1480, 190.2620, 320.7110.

1. INTRODUCTION

Nonlinear frequency conversion based on second-order nonlinear interactions in semiconductor optical waveguides is an attractive approach for creating compact, widely tunable, monolithically integrated, and efficient coherent light sources. In comparison, the wavelength coverage of available laser sources is restricted by inherent electronic transitions, leaving gaps in the spectrum, where no suitable material exists. Furthermore, solid-state laser sources have large table-top footprints and require careful alignment in comparison to monolithic diode lasers. As such, coherent radiations generated via nonlinear transitions have received much attention. The GaAs/AlGaAs material system is of particular interest for its large second-order nonlinearity ($d_{\mathrm{eff}}^{\mathrm{GaAs}} \approx 100$ pm/V around 1550 nm), broad transparency window (0.9–17 μm), and well-established fabrication technology. However, owing to their isotropic crystal structure, hence the lack of natural birefringence, phase-matching (PM) $\chi^{(2)}$ nonlinearities in AlGaAs devices generally involve significant challenges. Several techniques have been demonstrated to achieve PM such as artificial birefringence phase matching (BPM) [1–3], quasi-phase matching (QPM) [4,5], and modal phase matching (MPM) [6]. PM using Bragg reflection waveguides (BRWs) is another technique, akin to MPM, which utilizes the strong modal dispersion properties of photonic bandgap structures [7]. Unlike the conventional MPM, where attaining PM requires the involvement of higher order optical modes, BRWs offer exact PM between the lowest order modes, hence enabling maximum power utilization among the interacting frequencies. Also, the versatility along with the reduced fabrication complexity in BRWs is noteworthy. Unlike PM using birefringent waveguides, which involves invoking AlO_x elements within GaAs layers and QPM via domain reversal, which involves demanding overgrowth technology, PM using BRWs involves simple structures for epitaxial growth and well developed fabrication technologies. This in turn enables the realization of novel monolithically integrated parametric devices, where active elements such as diode laser pumps and diode photodetectors and passive elements such as nonlinear frequency mixing waveguides can be integrated on the same platform without the necessity of exploiting complex hybrid fabrication techniques. Further to being a powerful PM technique for dispersive semiconductors, BRWs also offer the ability of tuning pertinent waveguiding parameters, including overlap between the modal profiles of the interacting waves, bandgap, losses, group velocity mismatch (GVM), and group velocity dispersion (GVD), while maintaining PM. This in turn greatly enhances the ability to optimize the performance. Using BRWs, we can, not only obtain PM for any Al percentage and any bandgap desired, but also optimize the GVM and GVD along with the overlap between the modal profiles of the interacting waves, which relates the effective second-order nonlinear coefficient [8,9].

Practical $\chi^{(2)}$ nonlinear devices are essential elements

in many important applications in ultrafast optical signal processing. Examples include generation and detection of ultrashort optical pulses [10], characterization of ultrafast optical signals [11], as well as temporal control of optical signals [12]. Comprehensive understanding of $\chi^{(2)}$ nonlinear processes with ultrashort pulses in the different pulse-width regimes, such as those in the femtosecond region with moderate-to-high average powers, is not feasible without including the effects of modal dispersion properties as well as the effects of third-order optical nonlinearities. Although, the effects of $\chi^{(3)}$ nonlinearities such as two-photon absorption (TPA) and self-phase modulation (SPM) on second-order frequency mixing processes have been well established in the literature for bulk semiconductors and QPM waveguides [13–15], similar studies in BRWs have not been carried out. These studies can play an important role in the design of these structures due to the high degree of versatility they exhibit. Designs can be further enhanced by carefully tailoring the modal dispersion properties in BRWs particularly within the ultrashort pulse regime. The characterization of BRWs with picosecond pulses has been previously carried out and reported in the literature [16]. However, the effects of third-order nonlinearities were mildly manifested in this regime, owing to a moderate pump peak intensity. The employment of femtosecond pulses, where the pump peak intensity is significantly enhanced, can further highlight the effects of $\chi^{(3)}$ interactions on second-order processes, hence providing a more clear understanding of the potentials and limitations of these devices for optical frequency mixing.

The design optimization of BRWs for an efficient nonlinear interaction for the femtosecond pulsed regime is complex. This is because of the large number of parameters involved in the nonlinear process as well as the trade-offs associated. For example, the choice of the $Al_xGa_{1-x}As$ elements of the different BRW layers affects all dispersion orders, nonlinear coefficients, linear losses, nonlinear losses, as well as the optical field overlap factors. The versatile dispersion properties of BRWs can help decouple the aforementioned dependencies and enable performance optimization. The limitations and extent of the BRW capabilities will be investigated theoretically and experimentally in this work.

The organization of this paper is as follows. Section 2 provides an overview of the required theoretical background used for simulations and analysis. In Section 3, the simulation results are discussed, where detailed analyses of first- and second-order dispersion effects as well as the effects of $\chi^{(3)}$ nonlinearity on the second-harmonic generation (SHG) are presented. Section 4 provides the experimental results, where the pulse characterization of BRW devices in a SHG experiment with femtosecond pulses is carried out. Section 5 provides a comparative study between the femtosecond characterization of BRWs and other AlGaAs devices phase-matched using other techniques. Conclusions are summarized in Section 6.

2. THEORETICAL FRAMEWORK

In this section the theoretical framework, which describes the SHG process, is detailed. This provides the platform where numerous effects influencing the outcome SHG efficiency and hence the device design parameters are examined. The type II SHG can be regarded as a degenerate sum-frequency generation (SFG) involving the interactions of a transverse-magnetic (TM)-polarized pump (p_1), a transverse-electric (TE)-polarized pump (p_2), and a TE-polarized second-harmonic (SH) wave (i). The process is regarded as degenerate since the angular frequencies of the two pump waves are identical. We assume a collinear interaction in the waveguide along the z-axis and express the electric fields of the harmonics as

$$E_j(x,y,z,t) = A_j(z)E_j(x,y)\exp[-j(\beta_j z - \omega_j t)], \tag{1}$$

where $j \in \{p_1, p_2, i\}$; $A_j(z)$ is the slowly varying amplitude; ω_j is the angular frequency; $E_j(x,y)$ is the normalized spatial field profile; and β_j is the propagation constant, $\beta_j = 2\pi n_j/\lambda_j$, where n_j is the effective mode index and λ_j is the wavelength in vacuum. The evolution of slowly varying amplitudes, $A_j(z)$, along the propagation direction can be described by the couple-mode equations as [13,17]

$$\frac{dA_i}{dz} = -j\kappa_i \nu A_{p_1} A_{p_2} \exp[j\Delta\beta z] - \frac{1}{v_{g,i}}\frac{dA_i}{dt} - \frac{\alpha_{0,i}}{2}A_i - \left[\frac{\alpha_{2,i}}{2} - j\frac{2\pi n_{2,i}}{\lambda_i}\right]\frac{|A_i|^2}{A^{(3)}_{\text{eff},i}}A_i, \tag{2}$$

$$\frac{dA_{p_1}}{dz} = -j\kappa_{p_1} \nu^* A^*_{p_1} A_i \exp[-j\Delta\beta z] - \frac{1}{v_{g,p_1}}\frac{dA_{p_1}}{dt} - \frac{\alpha_{0,p_1}}{2}A_{p_1} - \left[\frac{\alpha_{2,p_1}}{2} - j\frac{2\pi n_{2,p_1}}{\lambda_{p1}}\right]\frac{|A_{p_1}|^2}{A^{(3)}_{\text{eff},p_1}}A_{p_1}, \tag{3}$$

$$\frac{dA_{p_2}}{dz} = -j\kappa_{p_2} \nu^* A^*_{p_2} A_i \exp[-j\Delta\beta z] - \frac{1}{v_{g,p_2}}\frac{dA_{p_2}}{dt} - \frac{\alpha_{0,p_2}}{2}A_{p_2} - \left[\frac{\alpha_{2,p_2}}{2} - j\frac{2\pi n_{2,p_2}}{\lambda_{p_2}}\right]\frac{|A_{p_2}|^2}{A^{(3)}_{\text{eff},p_2}}A_{p_2}, \tag{4}$$

where $\Delta\beta = \beta_i - \beta_{p_1} - \beta_{p_2}$ is the wave number mismatch; $v_{g,j}$ is the group velocity; ν is the spatial overlap factor; $\alpha_{0,j}$ is the linear loss coefficient; $\alpha_{2,j}$ and $n_{2,j}$ are the effective TPA and SPM coefficients of the structure, respectively; and $A^{(3)}_{\text{eff},j}$ is the third-order effective area. It is defined as

$$A^{(3)}_{\text{eff},j} = \frac{\left[\int_{-\infty}^{+\infty}\int_{-\infty}^{+\infty} I_j(x,y)\,dx\,dy\right]^2}{\int_{-\infty}^{+\infty}\int_{-\infty}^{+\infty} I_j^2(x,y)\,dx\,dy}, \tag{5}$$

where $I_j(x,y)$ is the transverse intensity profile. The pulse envelope is normalized such that the harmonic power P_j can be expressed as $P_j = |A_j|^2$. In Eqs. (2)–(4), the coupling coefficient κ_j is given by

$$\kappa_j = \left(\frac{8\pi^2 d_{\text{eff}}^2}{n_{p_1} n_{p_2} n_i c \epsilon_0 \lambda_j^2} \right)^{1/2}, \tag{6}$$

where d_{eff} is the effective second-order nonlinear coefficient, which is

$$d_{\text{eff}} = \frac{\int_{-\infty}^{+\infty} \int_{-\infty}^{+\infty} E_i^*(x,y) d(x,y) E_{p_1}(x,y) E_{p_2}(x,y) \mathrm{d}x\mathrm{d}y}{\int_{-\infty}^{+\infty} \int_{-\infty}^{+\infty} E_i^*(x,y) E_{p_1}(x,y) E_{p_2}(x,y) \mathrm{d}x\mathrm{d}y}, \tag{7}$$

where $d(x,y)$ is the effective $\chi^{(2)}$ coefficient for bulk AlGaAs elements [18,19].

In parametric processes involving ultrashort optical pulses, first- and second-order modal dispersions can considerably influence the efficiency of the nonlinear interaction. The first-order dispersion is generally quantified by the GVM, which accounts for the temporal pulse walk-off between the harmonics. Due to the mismatch between the group velocities among the interacting frequencies, the harmonics with an initial temporal overlap progressively undergo a temporal separation. For a type II interaction, by definition, GVMs between the orthogonal field components of pump (p_1,p_2) and SH signal are

$$\text{GVM}_{p_1,i} = \frac{1}{v_{g,p_1}} - \frac{1}{v_{g,i}}, \tag{8}$$

$$\text{GVM}_{p_2,i} = \frac{1}{v_{g,p_2}} - \frac{1}{v_{g,i}}. \tag{9}$$

Second-order modal dispersion properties can also have degrading effects on the efficiency of the nonlinear interaction. Of particular importance is the GVD, which manifests itself in the pulse broadening, hence reducing the pulse peak power. By definition, the GVD at ω_j frequency is given by

$$\text{GVD}_j = \frac{\partial^2 \beta_j}{\partial \omega^2} = \frac{2}{c}\frac{\partial n_j}{\partial \omega} + \frac{\omega_j}{c}\frac{\partial^2 n_j}{\partial \omega^2}, \tag{10}$$

where c is the vacuum speed of light.

The presence of third-order nonlinearities, including the TPA and SPM, under a high pump power condition can further impair the efficiency of the SHG. The TPA causes an increase in the absorption coefficient that is proportional to the intensity of the optical field. For the harmonic ω_j, the contribution of the TPA in increasing the loss coefficient of a bulk material is given by

$$\Delta\alpha_j = \alpha_{2,j} I_j. \tag{11}$$

For a waveguide structure, Eq. (11) can also be used provided that $\alpha_{2,j}$ is replaced with the effective TPA coefficient and I_j is replaced with the third-order nonlinear effective intensity [20].

An intensity dependence of the refractive index in nonlinear optical media occurs through the SPM, which leads to nonlinear phase shifting and spectral broadening of optical pulses. The changes in the refractive index Δn_j due to the SPM are given by

$$\Delta n_j = n_{2,j} I_j, \tag{12}$$

where, in a guided-wave structure, $n_{2,j}$ is the effective nonlinear refraction for the harmonic ω_j [20].

3. SIMULATION RESULTS

The aforementioned theory is now used to examine the effect of numerous parameters on the efficient SHG and hence the device design parameters, where two distinct sample designs are used to highlight the unintuitive design rules required for an efficient BRW design. In dispersive media such as semiconductors, the dispersion of the refractive index is sufficiently significant resulting in temporal walk-off between the input and the generated wavelengths, which reduces the conversion efficiency. Some of the most successful nonlinear materials such as periodically poled lithium niobate (PPLN) also exhibited severe limitations posed by the GVM such as pulse distortion and saturation effects when using femtosecond pulses [21]. Recently, GVM correction schemes such as quasi-group-velocity-matching [22] and noncollinear SHG [23] have been demonstrated in PPLN to mitigate these limitations. As such, we start by examining a BRW structure, with a minimal attainable GVM as an intuitive choice for an optimal design. After, an alternative design that utilizes the freedom of choice of the Al concentration afforded by PM using BRWs is used to demonstrate how the conversion efficiency can be increased at the expense of the GVM in short samples.

For numerically solving the coupled-mode equations of Eqs. (2)–(4), we employed the split-step Fourier method [15], where dispersion parameters as well as third-order nonlinear effects were included. Simulations were run such that the peak power of one wave remained fixed at $t=0$ while the other waves were allowed to change according to the differences in the group velocities. Two different structures, named BRW_I and BRW_II, have been comparatively studied in this section.

A. BRW_I

The initial structure has been optimized for having a minimal GVM with practical dimensions. The details of the waveguide geometry and how the optimization has been achieved for BRW_I have been published elsewhere [9]. A summary of all simulation parameters is given in Table 1, where $\alpha_{2,p_1(p_2)}$ and $n_{2,p_1(p_2)}$ were chosen from the maximum value of those in the layers of the structure. They were evaluated from [14,24,25].

The variation of the SH power as a function of the device length L is shown in Fig. 1. To be consistent in the comparison with experimental data, the pump average power P_{pump} ($P_{\text{pump}}=2P_{p_1}=2P_{p_2}$) was taken to be 3.3 mW in simulation. From the figure, it can be observed that the generated SH power increases with the increase in the sample length and then reaches the maximum value of 93 μW at $L=4.1$ mm. Further increase in L gives rise to a reduction in the SH power due to the adverse effects of linear propagation losses. Also in Fig. 1, the impacts of the TPA (α_2), SPM (n_2), GVM ($\text{GVM}_{p_1(p_2),i}$), and GVD ($\text{GVD}_{p_1(p_2)}$ and GVD_i) on the SH power were examined. From the figure, the existence of any of these four param-

Table 1. Simulation Parameters of BRW_I

Parameter	Value
Nonlinear interaction	Type I
$(\alpha_{0,p_1(p_2)}, \alpha_{0,i})$	(2.0,5.0)/cm
$\alpha_{2,p_1(p_2)}$	0.14 cm/GW
$n_{2,p_1(p_2)}$	3.5×10^{-5} cm^2/GW
$(A^{(3)}_{\text{eff},p_1(p_2)}, A^{(3)}_{\text{eff},i})$	(7.9,4.9) μm^2
d_{eff}	6.4 pm/V
$\text{GVM}_{p_1(p_2),i}$	−3.99 ps/mm
$\text{GVD}_{p_1(p_2)}$	1.24 fs^2/μm
GVD_i	−166 fs^2/μm
Pulse width	190 fs
Pulse repetition rate	76 MHz

eters will reduce the generated SH power. The impacts of the TPA and SPM are small under the low power levels of the pump and SH signal. Moreover, the GVD can degrade the maximum SH power by 73%, while the GVM degrades it by about 1.6 orders of magnitude. As such, it is believed that, in the femtosecond pulse regime, the major limiting factor in enhancing the SH power is the GVD and GVM between the pump and SH signal.

The nonlinear conversion efficiency defined as $\eta = P_i/P^2_{\text{pump}}$ and its value normalized to the square of the device length, $\eta_{\text{norm}} = P_i/(P_{\text{pump}}L)^2$, are two important figures of merit which characterize the waveguide performance in a SHG process. The variations of η and η_{norm} as functions of L are illustrated in Fig. 2. In obtaining the figures, the effects of the TPA, SPM, GVD, and GVM have been taken into consideration. The graph of η has the same trend as that of the SH power in Fig. 1, while η_{norm} exhibits a rapid reduction for sample lengths shorter than 500 μm after which it decreases with a slower slope. From Fig. 1, the simulated maximum SH power was obtained to be ≈2.2 μW for L=2.1 mm. The corresponding conversion efficiencies were estimated to be η=0.2% W^{-1} and η_{norm}=452% W^{-1} cm^{-2}. In the following simulations for BRW_I, the length of the sample was taken as 2.1 mm, because it agrees with the length of the tested samples.

In order to examine the effects of the SPM and TPA on the efficiency of the SHG process, we simulated the variations of η_{norm} as a function of the pump power for possible permutations of α_2 ($\alpha_{2,p_1(p_2)}$) and n_2 ($n_{2,p_1(p2)}$) with the effect of the GVM included. The results are shown in Fig. 3. From the figure, it can be seen that when both the SPM and TPA were ignored (n_2 off, α_2 off), the efficiency nearly does not change. Adding either the TPA (n_2 off, α_2 on) or SPM (n_2 on, α_2 off) conversion efficiency decreases with the increase in the pump power. For the case where both the SPM and TPA were included (n_2 on, α_2 on), the conversion efficiency dropped by 50% when the pump power was ≈25 mW. At pump powers lower than 3.3 mW, the degrading effects of third-order nonlinearities are within 3.6%.

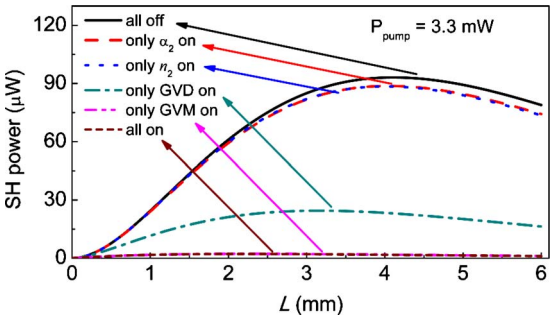

Fig. 1. (Color online) Simulated SH output power of BRW_I as a function of sample length where the effects of TPA with coefficient α_2, SPM with coefficient n_2, GVM, and GVD are independently included. All curves were obtained for a 190 fs pump with an average power of 3.3 mW.

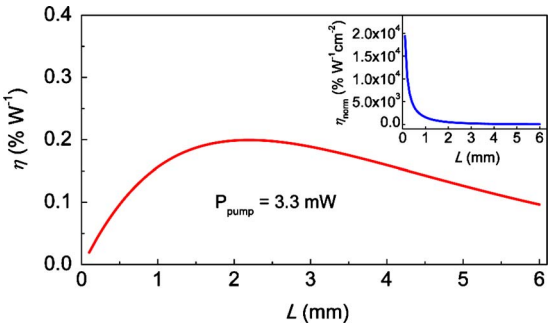

Fig. 2. (Color online) Simulated internal conversion efficiency η and normalized internal conversion efficiency η_{norm} (inset) of BRW_I as functions of sample length. The simulated graphs were obtained by including the effects of SPM, TPA, GVM, and GVD with their numerical values summarized in Table 1.

B. BRW_{II}

To further examine the potential of BRWs, another structure BRW_{II} with a higher GVM and with a higher effective second-order nonlinear coefficient has been designed. This can be afforded in BRWs with relative ease in comparison to other PM techniques, where limitations on the materials used and the operating wavelength relative to the material bandgap involve strict trade-offs. Details of the waveguide geometry of BRW_{II} were previously reported [16]. A summary of all the simulation parameters is given in Table 2, where the ridge width and etch depth of BRW_{II} were taken to be identical to those of BRW_I for a better comparison.

Figure 4 shows the variation of the SH power as a function of the device length for BRW_{II}. To be consistent with the experimental characterization launch conditions discussed in Section 4, the pump average power P_{pump} was taken to be 3.3 mW in the simulation. From the figure, it

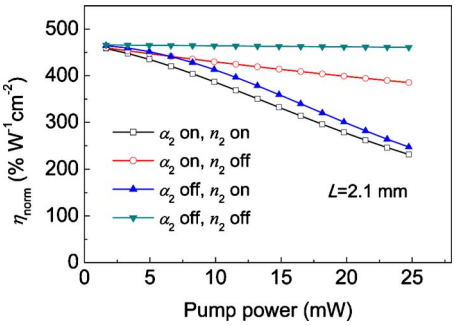

Fig. 3. (Color online) Effects of SPM (n_2) and TPA (α_2) on the normalized conversion efficiency (η_{norm}) of BRW_I as the pump power is increased.

Table 2. Simulation Parameters of BRW_{II}

Parameter	Value
Nonlinear interaction	Type II
$(\alpha_{0,p_1}, \alpha_{0,p_2}, \alpha_{0,i})$	(2.0,2.2,5.0)/cm
$(\alpha_{2,p_1}, \alpha_{2,p_2})$	(0.03,0.15) cm/GW
n_{2,p_1}	3.4×10^{-5} cm^2/GW
n_{2,p_2}	3.7×10^{-5} cm^2/GW
$(A^{(3)}_{\text{eff},p_1}, A^{(3)}_{\text{eff},p_2}, A^{(3)}_{\text{eff},i})$	(6.7,6.6,3.2) μm^2
d_{eff}	40.0 pm/V
$GVM_{p_1,i}$	−10.67 ps/mm
$GVM_{p_2,i}$	−10.63 ps/mm
GVD_{p_1}	5.65 $fs^2/\mu m$
GVD_{p_2}	5.65 $fs^2/\mu m$
GVD_i	170 $fs^2/\mu m$
Pulse width	190 fs
Pulse repetition rate	76 MHz

can be observed that the generated SH power increases as the sample length increases until it reaches the maximum value of 1.4 mW. Further increase in L gives rise to a reduction in the SH power due to the adverse effects of linear propagation losses. Also in Fig. 4, the impacts of the TPA (α_2), SPM (n_2), GVM ($GVM_{p_1,i}$ and $GVM_{p_2,i}$), and GVD (GVD_{p_1}, GVD_{p_2}, and GVD_i) on the SH power were examined. From the figure, the existence of any of these four parameters will reduce the generated SH power. The impacts of the TPA and SPM are small under the low power levels of the pump and SH signal. Moreover, the GVD can degrade the maximum SH power by 38%, while the GVM degrades it by about 1.3 orders of magnitude. However, the final maximum SH power is 69 μW at L = 1.5 mm when considering all the effects of the TPA, SPM, GVD, and GVM, which is about 31 times larger than that of BRW_I. This indicates that, even though the GVM and GVD are significant factors in limiting the SH power, they are not the only dominant factors. The second-order nonlinear coefficient also has a great effect on the conversion efficiency.

The variations of η and η_{norm} as functions of L are illustrated in Fig. 5, where all the effects of the TPA, SPM, GVD, and GVM have been taken into consideration. The maximum conversion efficiency η was about 6.2% W^{-1}; the corresponding η_{norm} was estimated to be 2.70×10^4% W^{-1} cm^{-2}. The characterized sample discussed in Section 4 had a length of L = 1.1 mm. From Fig. 4, the simulated SH power for a sample with the length of 1.1 mm was obtained to be 60 μW, which was in proximity to the maximum value of 69 μW. The corresponding normalized conversion efficiency was estimated to be $\eta_{\text{norm}} = 4.58\times10^4$% W^{-1} cm^{-2}. In the following simulations for BRW_{II}, the length of the sample was taken as close as practically possible to the calculated optimum and it was set to be 1.1 mm.

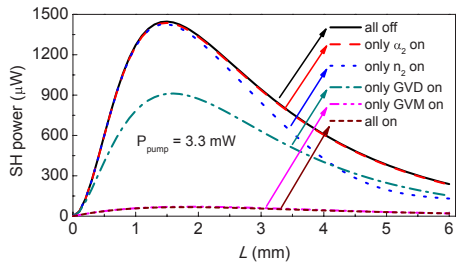

Fig. 4. (Color online) Simulated SH output power of BRW_{II} as a function of sample length, where the effects of TPA with coefficient α_2, SPM with coefficient n_2, GVM, and GVD are independently included. All curves were obtained for a 190 fs pump with an average power of 3.3 mW.

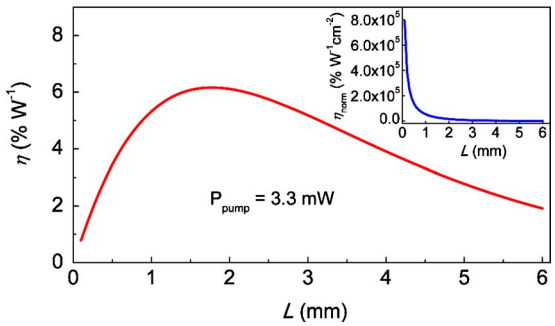

Fig. 5. (Color online) Simulated internal conversion efficiency η and normalized internal conversion efficiency η_{norm} (inset) of BRW_{II} as functions of sample length. The simulated graphs were obtained by including the effects of SPM, TPA, GVM, and GVD with their numerical values summarized in Table 2.

In order to examine the effects of the SPM and TPA on the efficiency of the SHG process, we simulated the variations of η_{norm} as functions of the pump power for possible permutations of α_2 ($\alpha_{2,p1}$ and $\alpha_{2,p2}$) and n_2 ($n_{2,p1}$ and $n_{2,p2}$) with the effect of the GVM included. The results are shown in Fig. 6. It can be seen that when both the SPM and TPA were ignored (n_2 off, α_2 off), the efficiency reduced solely due to the depletion of the pump power. Adding either the TPA (n_2 off, α_2 on) or SPM (n_2 on, α_2 off) had a similar behavior of the conversion efficiency, reducing as much as 16% at the pump power of ≈25 mW. At lower powers, the TPA attenuates the pump and has a larger effect on the efficiency than does the SPM. Above 6.6 mW, nonlinear phase shift and spectral broadening disturb the PM process and the SPM dominates in dropping the conversion efficiency. Finally, for the case where both the SPM and TPA were included (n_2 on, α_2 on), the conversion efficiency dropped by 20%. At pump powers lower than 3.3 mW, the effects of third-order nonlinearities degrade the power by 1.4% and can be ignored.

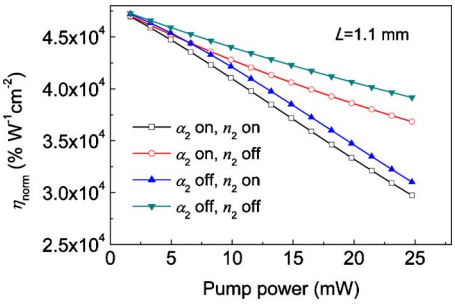

Fig. 6. (Color online) Effects of SPM (n_2) and TPA (α_2) on the normalized conversion efficiency (η_{norm}) of BRW_{II} as the pump power is increased.

From the numerical simulation results above, it can be seen that BRW_I cannot give us higher SH output powers and conversion efficiencies, although it benefits from the smaller first- and second-order dispersion compared to those in BRW_{II}. The relatively smaller effective second-order nonlinear coefficient of the structure limits the performance of BRW_I. As a result, in designing BRWs for ultrafast applications, trade-offs between various parameters including first- and second-order dispersion, third-order nonlinear effects, as well as the effective second-order nonlinear coefficient of the structure should all be carefully taken into consideration. As such waveguides identical to BRW_{II} were fabricated and characterized in the next section.

4. EXPERIMENTAL RESULTS

Detailed descriptions of the wafer used for the experiments (BRW_{II}) and its pulse characterization in the picosecond regime have been previously reported in [16]. The ridge waveguides studied here had a ridge width of 4.4 μm and an etch depth of 3.6 μm with a length of 1.1 mm. Propagation losses of the pump around 1550 nm were measured using the Fabry–Perot method and were found to be 2.0 and 2.2 cm^{-1} for the TE and TM components, respectively. The Fresnel reflection at the waveguide facets was estimated to be 29%. The input coupling factor due to the spatial overlap between the incident Gaussian beam and the excited pump mode was found to be 49%. Nonlinear characterization of the device was carried out using a homemade nearly transform-limited (with a temporal-spectral bandwidth product of $\Delta\tau\Delta\nu = 0.45$) optical parametric oscillator (OPO) able to provide efficient tunable femtosecond pulses in the near-infrared spectra. The OPO was based on a periodically poled $LiNbO_3$ [26] and was synchronously pumped by a commercial Kerr-lens-mode-locked Ti:sapphire laser at 814 nm, enabling the generation of pulses with a duration of 190 fs at a repetition rate of 76 MHz and continuously tunable around 1550 nm through adjustment of the cavity delay.

Figure 7 shows the internal SH power plotted as a function of the pump wavelength for the type II interaction and for the fixed internal pump power of 3.3 mW. From the figure, the corresponding PM wavelength was measured to be 1555 nm. The maximum SH power, estimated before the exit facet of the waveguide, was obtained to be 25.5 μW. The corresponding internal conversion efficiency was evaluated to be $2.0\times10^4\%$ W^{-1} cm^{-2}. However, the actual conversion efficiency is likely to be much higher given that more than 30% of the generated SHG power could not be collected due to the fast divergence of the BRW mode. Also given is that the internal pump power is overestimated based on the fact that the measured insertion loss value of −11 dB is much smaller than that estimated from linear loss measurement (−7 dB). The wavelength acceptance bandwidth, full width at half-maximum (FWHM), of the interaction was estimated to be 15.1 nm, which is comparable to that of the pump spectrum which is about 17.8 nm. In a recent work [27], a type II SFG process using a continuous-wave pump around the PM wavelength of 1555 nm was carried out on the device discussed here. In the aforementioned work, it was found that the FWHM bandwidth of the SFG process exceeds 60 nm. Considering the bandwidth of the femtosecond pump pulses in this work in addition to the large wavelength acceptance bandwidth of the SFG process, the SFG process may occur during the interactions. In order to determine the dominant nonlinear process in the characterization here, we examined the power dependence of the upconverted signal on that of the pump. The result is shown in the inset of Fig. 7, where the measured data are plotted on a log-log scale and are compared with a linear fit. The slope of the fit was obtained to be ≈1.75. From theory, it is well known that for the SHG the dependence of the SH power on that of the pump is quadratic, giving rise to a slope of 2 in log-log scale. On the other hand for the SFG, the powers of the pump and sum-frequency signal have a linear relationship resulting in a slope of unity in a log-log scale. Assuming that third-order nonlinearities can be neglected, the estimated slope of ≈1.75 in the inset of Fig. 7 clearly indicates that the dominant process in the measurement was indeed the SHG.

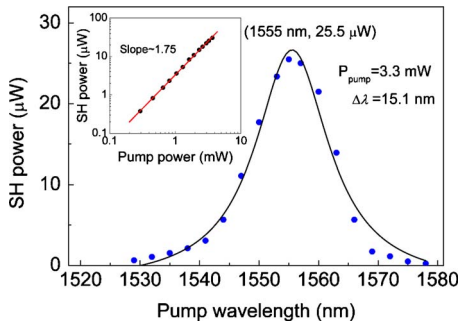

Fig. 7. (Color online) SH power as a function of pump wavelength for type-II interactions, the solid line is best fit to Lorentzian function. Inset: dependence of SH power on pump power plotted on log-log scale.

We further characterized waveguides with ridge widths ranging from 2.8–4.8 μm. Our measurements showed that, in all examined devices, the SH power was not sensitive to the ridge width of the waveguides. Also, for a longer sample with a length of 1.5 mm, the generated SH power was obtained to be ≈28.3 μW, denoting negligible enhancement compared to the obtained SH power of 25.5 μW in the sample with a length of 1.1 mm. The length dependence of the SH power agrees well with the calculations shown in Fig. 4. The discrepancy between the calculation and the experiment in estimating the SH power can be ascribed to the uncertainties involved in some of the simulation parameters including the SH loss, the structure d_{eff}, dispersion values, as well as the SPM and TPA coefficients used in the theoretical model.

The input and transmitted pump spectra at PM (1555 nm) and off PM (1575 nm) wavelengths are plotted in Fig. 8, where the solid curves show the input spectra while the dotted curves are those of the transmitted ones. From the figure, a clear dip can be observed in the transmitted spectra at the PM wavelength while no such dip can be observed away from the PM wavelength. The appearance of such a dip clearly indicates the depletion of the pump at the PM wavelength, where power transfer between the harmonics is the highest. It is worth noting that the SPM

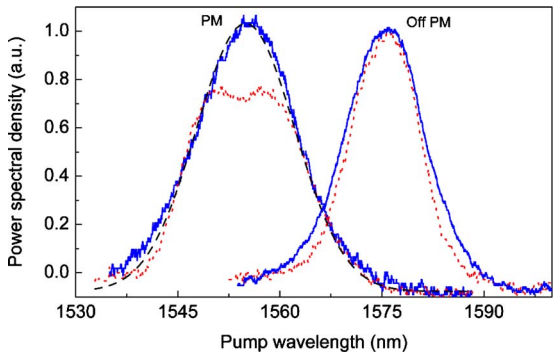

Fig. 8. (Color online) Normalized power spectral density of incident (solid curve) and transmitted (dotted curve) pumps for type-II interaction at PM and off PM wavelengths. The dashed curve is the Gaussian fitting of the transmitted spectrum at PM wavelength.

can also result in the appearance of a dip with distorted transmitted pump spectra. However, this possibility was dismissed by noticing that the bandwidths of the pump spectra at the input and output of the device were identical, denoting negligible spectral broadening due to the SPM. Also, during the experiment, it was noted that changing the central pump wavelength within the pump bandwidth did not change the position of the dip in the transmitted pump spectra which further confirmed the existence of the pump depletion taking place around the PM wavelength.

5. DISCUSSION

The attributes of PM using BRW waveguides come to light once their SHG performance is compared with their counterparts. A comparison among some previously reported femtosecond SHGs using different PM techniques is provided in Table 3. For the referenced QPM and MPM samples in Table 3 the characterization was carried out using 250 fs pulses, while the BPM device was characterized using 200 fs pulses. From Table 3 it can be seen that nonlinear interaction in our device is more efficient compared to QPM and MPM devices. However, in comparison to BPM waveguide, our device is less efficient by less than 1 order of magnitude. It should be highlighted that the reported SH power of BRW_{II} defined a lower limit for the generated SH signal. This can be justified by noticing that in estimating the SH power, we assumed perfect collection through the output stage objective lens. In reality, part of the beam could not be collected due to fast divergence of the emerging beam from the waveguide facet. As such, we believe that in terms of the signal to noise ratio and the efficiency of the nonlinear interaction, our reported device is in vicinity of well-established phase-matched $Al_xGa_{1-x}As$ waveguides. The advantages of using phase-matched BRWs in the femtosecond regime can be further enhanced by utilizing the flexibility afforded by the BRW in choosing the material bandgap in comparison to the operating wavelength, which is compensated by the strong waveguide dispersion properties of these devices. For example, in the choice of material for the BPM sample in [3] the required birefringence could only be obtained between GaAs and AlO_x elements. While the employment of AlO_x layers could limit the practicality of BPM devices for integration with diode laser pumps, where electric pumping is required, the choice of GaAs layers with material resonances around 870 nm could further limit their useful spectral range for optical frequency mixing. In contrast, BRWs avoid such limitations, which make them promising for novel parametric devices. The comparison suggests that the samples tested in the previous section may provide a near optimum performance given the practical limitations of the epitaxial growth and waveguide fabrication in this material system.

Table 3. Comparison of Efficiencies Obtained for Various Samples Using Different PM Techniques. The Extensions-I and -II Indicate Types I and II PMs, Respectively

Sample	Length (mm)	P_{FH} (mW)	P_{SH} (μW)	P_{SH}/P_{FH} (%)
QPM-I [28]	4.0	2.3	0.11	0.02
QPM-I [29]	2.0	11	1.5	0.06
MPM-II [6]	1.5	20	10.3	0.15
BPM-I [3]	1.0	50	650	1.3[a]
BRW_{II}-II	1.1	3.3	25.5	0.77

[a]External efficiency.

6. CONCLUSIONS

Using the split-step Fourier method, the impact of third-order nonlinearities including the SPM and TPA on the efficiency of the SHG is numerically investigated. Furthermore, the adverse effects of the GVM and GVD of the interacting frequencies on the efficiency of the nonlinear process are studied using the same method. Using the optimized designs inferred from these studies, we have demonstrated an efficient SHG in Bragg reflection waveguides (BRWs) using femtosecond pulses. Pump depletion was observed in a waveguide with a length of 1.1 mm in a type II interaction. The peak SH power of 25.5 μW was estimated for a pump power of 3.3 mW around 1555 nm. The normalized internal conversion efficiency of the process was estimated to be 2.0 $\times 10^4$% W^{-1} cm^{-2}. Theoretical simulations indicated that pulse walk-off due to the GVM between the pump and SH signal was the main limitation in enhancing the SH power, hence limiting the efficiency of the nonlinear interaction.

ACKNOWLEDGMENTS

The authors gratefully acknowledge the support of the Ontario Centres of Excellence (OCE), Institut de Ciencies Fotoniques (ICFO), the Consolider project (SAUUL) Natural Sciences and Engineering Research Council of Canada (NSERC), and CMC Microsystems.

REFERENCES

1. A. Fiore, V. Berger, E. Rosencher, P. Bravetti, and J. Nagle, "Phase matching using an isotropic nonlinear optical material," Nature **391**, 463–466 (1998).
2. M. Ravaro, M. L. Dû, J. P. Likforman, S. Ducci, V. Berger, G. Leo, and X. Marcadet, "Estimation of parametric gain in

GaAs/AlO_x waveguides by fluorescence and second harmonic generation measurements," Appl. Phys. Lett. **91**, 191110 (2007).
3. K. Moutzouris, S. Venugopal Rao, M. Ebrahimzadeh, A. De Rossi, V. Berger, M. Calligaro, and V. Ortiz, "Efficient second-harmonic generation in birefringently phase-matched GaAs/Al_2O_3 waveguides," Opt. Lett. **26**, 1785–1787 (2001).
4. S. J. B. Yoo, R. Bhat, C. Caneau, and M. A. Koza, "Quasi-phase-matched second-harmonic generation in AlGaAs waveguides with periodic domain inversion achieved by wafer-bonding," Appl. Phys. Lett. **66**, 3410–3412 (1995).
5. X. Yu, L. Scaccabarozzi, J. S. Harris, P. S. Kuo, and M. M. Fejer, "Efficient continuous wave second harmonic generation pumped at 1.55 μm in quasi-phase-matched AlGaAs waveguides," Opt. Express **13**, 10742–10748 (2005).
6. K. Moutzouris, S. V. Rao, M. Ebrahimzadeh, A. De Rossi, M. Calligaro, V. Ortiz, and V. Berger, "Second-harmonic generation through optimized modal phase matching in semiconductor waveguides," Appl. Phys. Lett. **83**, 620–622 (2003).
7. A. S. Helmy, B. Bijlani, and P. Abolghasem, "Phase matching in monolithic Bragg reflection waveguide," Opt. Lett. **32**, 2399–2401 (2007).
8. A. S. Helmy, "Phase matching using Bragg reflection waveguides for monolithic nonlinear optics applications," Opt. Express **14**, 1243–1252 (2006).
9. P. Abolghasem and A. S. Helmy, "Matching layers in Bragg reflection waveguides for enhanced nonlinear interaction," IEEE J. Quantum Electron. **45**, 646–653 (2009).
10. V. Petrov, M. Ghotbi, O. Kokabee, A. Esteban-Martin, F. Noack, A. Gaydardzhiev, I. Nikolov, P. Tzankov, I. Buchvarov, K. Miyata, A. Majchrowski, I. V. Kityk, F. Rotermund, E. Michalski, and M. Ebrahim-Zadeh, "Femtosecond nonlinear frequency conversion based on BiB_3O_6 ," Laser Photonics Rev. **4**, 53–98 (2010).
11. A. Galvanauskas, J. Webjorn, A. Krotkus, and G. Arvidsson, "Autocorrelation measurement of picosecond laser-diode pulses by means of quasiphase-matching $LiNbO_3$ channel waveguides," Electron. Lett. **27**, 738–740 (1991).
12. T. Suhara and H. Ishizuki, "Integrated QPM sum-frequency generation interferometer device for ultrafast optical switching," IEEE Photon. Technol. Lett. **13**, 1203–1205 (2001).
13. S. J. Wagner, A. A. Muhairi, J. S. Aitchison, and A. S. Helmy, "Modeling and optimization of quasi-phase matching via domain-disordering," IEEE J. Quantum Electron. **44**, 424–429 (2008).
14. J. S. Aitchison, D. C. Hutchings, J. U. Kang, G. I. Stegeman, and A. Villeneuve, "The nonlinear optical properties of AlGaAs at the half band gap," IEEE J. Quantum Electron. **33**, 341–348 (1997).
15. G. P. Agrawal, *Nonlinear Fiber Optics*, 2nd ed. (Academic, 1995).
16. P. Abolghasem, J. Han, A. Arjmand, B. Bijlani, and A. S. Helmy, "Highly efficient second-harmonic generation in monolithic matching-layer enhanced $Al_xGa_{1-x}As$ Bragg reflection waveguides," IEEE Photon. Technol. Lett. **21**, 1462–1464 (2009).
17. R. V. Roussev, C. Langrock, J. R. Kurz, and M. M. Fejer, "Periodically poled lithium niobate waveguide sum-frequency generation for efficient single-photon detection at communication wavelengths," Opt. Lett. **29**, 1518–1520 (2004).
18. M. Ohashi, T. Kondo, R. Ito, S. Fukatsu, Y. Shiraki, K. Kumata, and S. S. Kano, "Determination of quadratic nonlinear optical coefficient of $Al_xGa_{1-x}As$ system by the method of reflected second harmonics," J. Appl. Phys. **74**, 596–601 (1993).
19. I. Shoji, T. Kondo, A. Kitamoto, M. Shirane, and R. Ito, "Absolute scale of second-order nonlinear-optical coefficients," J. Opt. Soc. Am. B **14**, 2268–2294 (1997).
20. R. S. Grant, "Effective non-linear coefficients of optical waveguide," Opt. Quantum Electron. **28**, 1161–1173 (1996).
21. Z. Zheng, A. M. Weiner, K. R. Parameswaran, M. H. Chou, and M. M. Fejer, "Femtosecond second-harmonic generation in periodically poled lithium niobate waveguides with simultaneous strong pump depletion and group-velocity walk-off," J. Opt. Soc. Am. B **19**, 839–848 (2002).
22. J. P. Xie, J. Huang, and M. M. Fejer, "Narrow-linewidth near-degenerate optical parametric generation achieved with quasi-group-velocity-matching in lithium niobate waveguides," Opt. Lett. **31**, 2190–2192 (2006).
23. N. Fujioka, S. Ashihara, H. Ono, T. Shimura, and K. Kuroda, "Group-velocity-matched noncollinear second-harmonic generation in quasi-phase matching," J. Opt. Soc. Am. B **22**, 1283–1289 (2005).
24. B. S. Wherrett, "Scaling rules for multiphoton interband absorption in semiconductors," J. Opt. Soc. Am. B **1**, 67–72 (1984).
25. M. Sheik-Bahae, D. C. Hutchings, D. J. Hagan, and E. W. Van Stryland, "Dispersion of bound electron nonlinear refraction in solids," Opt. Quantum Electron. **27**, 1296–1309 (1991).
26. A. Esteban-Martin, O. Kokabee, and M. Ebrahim-Zadeh, "Efficient, high-repetition-rate, femtosecond optical parametric oscillator tunable in the red," Opt. Lett. **33**, 2650–2652 (2008).
27. J. Han, P. Abolghasem, B. J. Bijlani, and A. S. Helmy, "Continuous-wave sum-frequency generation in AlGaAs Bragg reflection waveguides," Opt. Lett. **34**, 3656–3658 (2009).
28. A. S. Helmy, D. C. Hutchings, T. C. Kleckner, J. H. Marsh, A. C. Bryce, J. M. Arnold, C. R. Stanley, J. S. Aitchison, C. T. A. Brown, K. Moutzouris, and M. Ebrahimzadeh, "Quasi phase matching in GaAs-AlAs superlattice waveguides through bandgap tuning by use of quantum-well intermixing," Opt. Lett. **25**, 1370–1372 (2000).
29. K. Zeaiter, D. C. Hutchings, R. M. Gwilliam, K. Moutzouris, S. Venugopal Rao, and M. Ebrahimzadeh, "Quasi-phase-matched second-harmonic generation in a GaAs/AlAs superlattice waveguide by ion-implantation-induced intermixing," Opt. Lett. **28**, 911–913 (2003).